Supplementary Information for

Electrocatalytic upcycling of high-pressure captured CO_2

Liang Huang,[1] Ge Gao,[1] Jiwu Zhao,[1] William L. Roberts,[1] Xu Lu[1]*

[1]Division of Physical Science and Engineering (PSE), King Abdullah University of Science and Technology (KAUST), Thuwal, 23955-6900, Kingdom of Saudi Arabia.

*Corresponding author. Email: Xu Lu (xu.lu@kaust.edu.sa).

This PDF file includes:

Materials and Methods

Catalyst synthesis

To synthesize In_1/Cu, 100 mg of copper(II) acetate (Sigma-Aldrich, 99.9%) and 3 mg of indium(III) acetate (Sigma-Aldrich, 99.99%) were first added to 300 mL of H_2O (Milli-Q Water System, 18.2 MΩ·cm). Then, 5 mL of NaOH (100 mM, Sigma-Aldrich, 98%) aqueous solution was added dropwise under stirring. Next, 10 mL of hydrazine hydrate (Sigma-Aldrich, N_2H_4 50-60 %) was added to the flask and stirred at 50°C for 1 hour. The precipitate was subsequently washed multiple times by centrifugation with H_2O and ethanol before being dried in a vacuum oven. The powder was placed in a tube furnace and heated at 240°C for 2 hours under an H_2/Ar (5% H_2, Air Liquide) mixture atmosphere, and finally the In_1/Cu catalyst was obtained. The synthetic procedures were similar for Ag_1/Cu and Al_1/Cu catalysts, except for the use of 1.7 mg of silver acetate (Sigma-Aldrich, 99%) and 2.4 mg of aluminum chloride (Sigma-Aldrich, 99.99%) as the precursor, respectively.

Physical characterizations

Scanning electron microscopy (SEM) images were collected using FEI Quanta 600 FEG ESEM operated at 20 kV. Transmission electron microscopy (TEM) images were acquired using FEI Tecnai G^2 Spirit Twin operated at 120 kV. High-resolution TEM (HRTEM), scanning TEM (STEM), and electron energy loss spectroscopy (EELS) were performed by FEI Titan 80-300 equipped with a field emission gun and spherical aberration corrector operated at 300 kV. EELS mapping was collected using a post-column filter in diffraction mode. X-ray photoelectron spectroscopy (XPS) was operated using Kratos Analytical AMICUS/ESCA 3400 equipped with an Mg-anode Kα excitation X-ray source ($h\nu$ = 1253.6 eV) at 10 kV, 10 mA, and 2×10^{-6} Pa. The binding energies were calibrated based on C 1*s* binding energy at 284.8 eV. Powder X-ray powder diffraction (XRD) was carried out using the Bruker D8 Advance with a Cu Kα radiation. X-ray absorption spectroscopy (XAS) was measured at the beamline BL14W station of the Shanghai Synchrotron Radiation Facility with an electron beam energy of 3.5 GeV and a ring current of 200–300 mA. The X-ray absorption fine structure (XAFS) and X-ray absorption near-edge structure (XANES) spectra of the Cu K-edges were recorded in a fluorescence mode, with Cu foil and CuO as references. The hard X-ray was monochromatized with Si (111) double-crystals. The acquired EXAFS data were extracted and processed according to the standard procedures using the ATHENA module implemented in the IFEFFIT software packages.

Electrode preparation

Membrane electrode assembly (MEA) was fabricated by a catalyst-coated membrane (CCM)

technique. First, two different catalyst inks were prepared for the cathode: Ink 1 comprised 10 mg of M_1/Cu catalysts and 70 μL of anion-exchange ionomer (PiperION-A5, 5 wt%, Versogen) in 10 mL of isopropanol, while Ink 2 contained 10 mg of M_1/Cu catalysts, 30 μL of PiperION ionomer, 5 μL of polytetrafluoroethylene (PTFE) solution (60 wt % dispersion in H_2O, Sigma-Aldrich) and 4 mg of graphitized carbon nanotubes (30-50 nm, Aladdin, 99.9%) in 10 mL of isopropanol. Following 2 h sonication, 1 mL of ink 1 and ink 2 were spray-coated sequentially onto the central area (1× 1 cm^2) of the anion-exchange membrane (PiperION-A20-HCO_3, 20 μm thick, Versogen) to create the cathode catalyst layer. Subsequently, the cathode catalyst-coated membrane was sandwiched by a PTFE-treated carbon paper gas diffusion layer (GDL) and a Ni-Fe hydroxide electrodeposited Ni foam anode[1]. Finally, the sandwich assembly was hot-pressed at 70°C and 1000 psi for 2 minutes to form a MEA (Supplementary Fig. 2).

High-pressure captured CO_2

High-pressure captured CO_2 (HP-cCO_2) was sourced from a Cryogenic Carbon Capture (CCC) rig at KAUST[2]. The low-temperature purified liquid CO_2 (>99.99%) from the distillation tank of CCC (10 bar, -50 °C) was conveniently regulated to a room-temperature compressed gas phase up to 73 bar without additional energy consumption (Supplementary Fig. 19). HP-cCO_2 flowed into the MEA reactor for electrolysis as controlled by a high-pressure mass flow controller (MFC, Beijing Scistar Technology Co. Ltd).

Electrochemical CO_2 reduction

The gas-phase high-pressure CO_2 electroreduction system consisted of a homemade MEA electrolyzer, a high-pressure high-performance liquid chromatography pump (HPLC pump, Sanotac SP6010), a high-pressure mass flow controller, three backpressure valves (Beijing Xiong Chuan Technology Co. LTD) and three Teflon-lined titanium tanks (Supplementary Fig. 1). The as-prepared MEA was fixed and sealed between two titanium polar plates with channels and ports, forming a MEA electrolyzer. During electrochemical testing, the cathode was supplied with humidified HP-cCO_2, while the anode was supplied with pressurized CO_2 saturated $KHCO_3$ (0.1 M) aqueous solution. Backpressure valves regulated pressures on both cathode and anode sides to maintain the equilibrium. MFC and HPLC pump controlled the HP-cCO_2 and anolyte flow rates at 120 mL min^{-1} and 30 mL min^{-1}, respectively. All electrochemical measurements were conducted using a BioLogic SP-150 potentiostat. Full-cell voltages of the MEA were measured using the chronopotentiometry method. The currents were normalized to the geometric area of the working electrodes.

Product analysis

Gas streams from both cathode and anode were analyzed online using a gas chromatograph (GC, Trace 1310, Thermo Scientific) equipped with Molecular Sieve 5A and Porapak N columns. Ar (Al Khafrah Industrial Gases, 99.999%) was used as the carrier gas. CO, CH_4, C_2H_4, C_2H_6, C_3H_6, and C_3H_8 were quantified using a flame ionization detector (FID) with a methanizer. H_2 and CO_2 were quantified using a thermal conductivity detector (TCD). The concentrations of gas products were derived from the output peak areas based on calibration curves. Liquid effluents from both cathode and anode were collected and analyzed by a ^{1}H NMR (Bruker, 600 MHz) using a water suppression method. Each NMR sample was prepared by mixing 490 μL of the collected solutions with 110 μL of the internal standards (20 ppm of dimethyl sulfoxide in D_2O).

Operando Raman spectroscopy

Operando Raman spectroscopy was conducted in a customized high-pressure MEA electrolyzer, equipped with a sapphire optical window. The MEA consisted of a catalyst-coated AEM, a carbon paper GDL with laser-engraved micropores (diameter: 50 μm), and a IrO_2/Ti meshed anode (400 mesh), assembled via hot pressing. The CCM technique ensures the integrity of the cathode catalyst layer (thickness: 1 μm). The laser and Raman signals can penetrate through the optical window, the cathodic serpentine flow field, and the micropores of the GDL onto the catalyst layer. The Raman spectrometer can also focus on the catalyst-AEM interface through the anodic Titanium mesh (Fig. 3a and Supplementary Fig. 17). The Raman spectra were recorded using a WITec apyron system equipped with a 633 nm He-Ne laser beam, a ×50 objective (NA = 0.55), and a CCD detector. The acquisition time was 20 s for each spectrum with the accumulation times of 2.

Computational details

The DFT and *Ab initio* molecular dynamic (AIMD) calculations were performed on Vienna *Ab initio* Simulation Package (VASP) code[3,4]. The interaction of core and electrons was treated by projector augmented wave (PAW) pseudopotential[5,6] with a cut-off energy of 550 eV. The exchange-correlation function was described by the generalized-gradient approximation-Perdew-Burke-Ernzerhof (GGA-PBE)[7]. The DFT-D3(BJ) method was used to consider the vdW-dispersion energy-correction[8]. Convergence in geometry optimization was reached when the force on each atom fell below 0.02 eV Å^{-1}.The molecular density in the vacuum layer (10 Å) was assumed to be 1 and 10 nm^{-3} for ambient and high-pressure conditions, respectively. The Brillouin zone sampling was performed using Gamma-centered Monkhorst-Pack (MP) grids[9], and the k-point was set as 3×3×1

for all the DFT calculations. The data processing was facilitated by VASPKIT[10], QVASP[11] and VESTA[12] software. The Gibbs free energy difference (ΔG) between initial and final states was denoted as:

$$\Delta G = \Delta E + \Delta ZPE - T\Delta S$$

where E, ZPE, T and S represent the energy from DFT calculation, zero-point energy, temperature (298.15 K) and entropy, respectively[13,14]. Our calculation followed a commonly recognized CO_2R mechanism[15,16]: CO was first reduced to *CO via *COOH, and then hydrogenated to *COH; subsequently, *COH couples with *CO to form *HOCCO*, which undergoes hydrodeoxygenation to release C_2H_4 via proton-coupled electron transfer.

Techno-economic analysis

The techno-economic analysis (TEA) was performed based on prior work[17-19] to explore the economic feasibility of producing C_2H_4 from HP-cCO_2 assuming a 20-year factory life.

Assuming a daily C_2H_4 production of 100 tons, the C_2H_4 production rate is:

$$C_2H_4 \text{ production rate } (\frac{\text{mol}}{\text{s}}) = \frac{C_2H_4 \text{ production } (\frac{\text{g}}{\text{day}})}{\text{Molar mass}_{C_2H_4} (\frac{\text{g}}{\text{mol}}) \times 86400 (\frac{\text{s}}{\text{day}})}$$

The required total current is:

$$\text{Total current (A)} = \frac{C_2H_4 \text{ production rate} \times \text{Electrons transferred} \times \text{Faraday Constant}}{\text{FE}}$$

The required power is:

$$\text{Power (W)} = \text{Total current (A)} \times \text{Cell voltage (V)}$$

Electricity cost:

The electricity cost per 100 tons of C_2H_4 production is calculated via multiplying the power consumption by 24 hours and renewable electricity price ($0.02/kWh)[19].

$$\text{Electricity cost (\$)} = \text{Power (W)} \times 24 \text{ h} \times \text{electricity price (\$/kWh)}$$

Electrolyzer cost:

With a reference electrolyzer cost of $250/kW and a reference current density of 200 mA cm^{-2},[18,20,21] our total electrolyzer cost was estimated via scaling the electrolyzer unit price by the ratio of the reference current density versus our input current density.

$$\text{Total electrolyzer cost (\$)} = \text{Power (kW)} \times \text{Electrolyzer cost (\$)} \times \frac{\text{Reference current density } (\frac{\text{mA}}{\text{cm}^2})}{\text{Input current density } (\frac{\text{mA}}{\text{cm}^2})}$$

The above one-time total electrolyzer cost needs to be converted to a cost per ton of C_2H_4 using a capital recovery factor (CRF) based on a discount rate (i = 0.07) and the lifetime of the materials:

$$\mathrm{CRF_{electrolyzer}} = \frac{\mathrm{i(1+i)^{lifetime}}}{\mathrm{(1+i)^{lifetime}-1}}$$

Assuming a plant capacity factor of 0.9, the electrolyzer cost per ton of C_2H_4 is:

$$\text{Electrolyzer cost } (\frac{\$}{\mathrm{ton_{C_2H_4}}}) = \frac{\mathrm{CRF_{electrolyzer}} \times \text{Total electrolyzer cost (\$)}}{\text{Capacity factor} \times 365 \left(\frac{\text{days}}{\text{year}}\right) \times \mathrm{C_2H_4} \text{ production } (\frac{\text{ton}}{\text{day}})}$$

Catalyst and membrane cost:

Assuming that the catalyst and membrane (C&M) account for 5% of the total electrolyzer cost with a lifetime of 5 years, the catalyst and membrane cost per ton of C_2H_4 is:

$$\mathrm{CRF_{C\&M}} = \frac{\mathrm{i(1+i)^{lifetime}}}{\mathrm{(1+i)^{lifetime}-1}}$$

$$\mathrm{Cost_{C\&M}} \ (\frac{\$}{\mathrm{ton_{C_2H_4}}}) = \frac{\mathrm{CRF_{C\&M}} \times \text{Total electrolyzer cost (\$)} \times 5\%}{\text{Capacity factor} \times 365 \ (\frac{\text{days}}{\text{year}}) \times \mathrm{C_2H_4} \text{ production } (\frac{\text{ton}}{\text{day}})}$$

Product separation:

Gas product separation with a pressure swing adsorption (PSA) separation unit: Costs are calculated using a model incorporating the capital and operating expenses. The model is based on a reference cost of \$1,989,043 for a flowrate capacity of 1000 m^3/hour, scaled by a factor of 0.7, and with an energy consumption of 0.25 kWh/m^3.[18,22]

$$\text{PSA Capital Cost (\$)} = \$1989043 \times (\frac{\text{Flow rate } (\frac{\mathrm{m^3}}{\text{hour}})}{1000 \frac{\mathrm{m^3}}{\text{hour}}})^{0.7}$$

$$\text{PSA Operating Cost (\$)} = 0.25 \frac{\text{kWh}}{\mathrm{m^3}} * \text{Flowrate } (\frac{\mathrm{m^3}}{\text{hour}}) \times 24 \frac{\text{hour}}{\text{day}} \times \text{Electricity price } (\frac{\$}{\text{kWh}})$$

$$\text{Output } \mathrm{C_2H_4} \text{ flowrate } (\frac{\mathrm{m^3}}{\text{hour}}) = \frac{\mathrm{nRT}}{\mathrm{P} \times 24 \frac{\text{hour}}{\text{day}}} = \frac{\frac{\mathrm{m}}{\mathrm{M}}\mathrm{RT}}{\mathrm{P} \times 24 \frac{\text{hour}}{\text{day}}}$$

$$\text{Output } \mathrm{CO_2} \text{ flowrate } (\frac{\mathrm{m^3}}{\text{hour}}) = \frac{\mathrm{C_2H_4} \text{ flowrate } (\frac{\mathrm{m^3}}{\text{hour}}) \times \text{molar ratio} (\frac{\mathrm{CO_2}}{\mathrm{C_2H_4}})}{\text{single pass conversion}} \times (1 - \text{single pass conversion})$$

$$\text{Output } \mathrm{H_2} \text{ flowrate } (\frac{\mathrm{m^3}}{\text{hour}}) = \frac{\mathrm{H_2} \text{ production } (\frac{\text{mol}}{\text{hour}}) \times \mathrm{RT}}{\mathrm{P}} = \frac{\mathrm{H_2} \text{ current } (A) \times 3600 \frac{\mathrm{s}}{\text{hour}}}{2 \frac{\text{electrons}}{\mathrm{H_2} \text{ product}} \times \text{Faraday Constant}} \times \frac{\mathrm{RT}}{\mathrm{P}}$$

where R = 8.314 J mol^{-1} K^{-1}, T = 298 K and P = 101300 Pa.

$$\text{Total flowrate} = \text{Output } \mathrm{CO_2} \text{ flowrate} + \text{Output } \mathrm{C_2H_4} \text{ flowrate} + \text{Output } \mathrm{H_2} \text{ flowrate}$$

With the total flowrate, we can calculate the capital and operating cost:

$$\text{PSA operating cost } \left(\frac{\$}{\text{ton}_{C_2H_4}}\right)$$

$$= \frac{0.25\,\frac{\text{kWh}}{\text{m}^3} \times \text{Total flowrate } \left(\frac{\text{m}^3}{\text{hour}}\right) \times 24\,\frac{\text{hour}}{\text{day}} \times \text{Electricity price } \left(\frac{\$}{\text{kWh}}\right)}{C_2H_4 \text{ production } \left(\frac{\text{ton}}{\text{day}}\right)}$$

$$\text{PSA capital cost } \left(\frac{\$}{\text{ton}_{C_2H_4}}\right) = \frac{\text{CRF}_{\text{electrolyzer}} \times \text{PSA capital cost } (\$)}{\text{Capacity factor} \times 365\,\frac{\text{day}}{\text{year}} \times C_2H_4 \text{ production } \left(\frac{\text{ton}}{\text{day}}\right)}$$

$$\text{Gas separation cost } \left(\frac{\$}{\text{ton}_{C_2H_4}}\right) = \text{PSA operating cost } \left(\frac{\$}{\text{ton}_{C_2H_4}}\right) + \text{PSA capital cost } \left(\frac{\$}{\text{ton}_{C_2H_4}}\right)$$

Gas product separation with a CCC rig: CCC cools exhaust gases to isolate frozen CO_2. The distinct physical properties and phase transitions of CO_2, C_2H_4 and H_2 enable the CCC rig, with its desublimating heat exchanger and three-phase separator, to efficiently separate CO_2R effluent into different phases, thereby extracting high-purity C_2H_4 and recycling CO_2. The corresponding gas separation cost is calculated as follows:

$$\text{Gas separation cost with CCC } \left(\frac{\$}{\text{ton}_{C_2H_4}}\right)$$

$$= \frac{\text{CCC operating cost } \left(\frac{\$}{\text{ton}_{CO_2}}\right) \times CO_2 \text{ mass fraction in flue gas} \times \text{Total flowrate } \left(\frac{\text{ton}}{\text{day}}\right)}{CO_2 \text{ mass fraction in } CO_2\text{R effluent} \times C_2H_4 \text{ production } \left(\frac{\text{ton}}{\text{day}}\right)}$$

Chemical costs:

Assuming a fixed volume ratio of 100 L electrolyte (0.1 M $KHCO_3$) per m^2 of electrolyzer, a price of 750 \$/ton for $KHCO_3$ and a price of 5 \$/ton for water,[18] the cost of input chemicals is calculated as follows:

$$\text{Volume}_{\text{electrolyte}} \text{ (L)} = \text{Surface area } (\text{m}^2) \times 100\,\frac{\text{L}}{\text{m}^2} = \frac{\text{Total current (mA)}}{\text{Current density } \left(\frac{\text{mA}}{\text{cm}^2}\right) \times \left(\frac{100\text{ cm}}{1\text{ m}}\right)^2} \times 100\,\frac{\text{L}}{\text{m}^2}$$

$$\text{Mass}_{\text{salt}} \text{ (g)} = \text{Molarity}_{\text{salt}} \left(\frac{\text{mol}}{\text{L}}\right) \times \text{Volume}_{\text{electrolyte}} \text{ (L)} \times \text{Molar mass } \left(\frac{\text{g}}{\text{mol}}\right)$$

$$\text{Cost}_{\text{electrolyte}}(\$)$$

$$= \text{Mass}_{\text{salt}}(\text{tons}) \times \text{price of salt } \left(\frac{\$}{\text{ton}}\right)$$

$$+ \text{Volume}_{\text{water}} \text{ (L)} \times \text{Density}_{\text{water}} \left(\frac{\text{kg}}{\text{L}}\right) \times \text{water price } \left(\frac{\$}{\text{kg}}\right)$$

To obtain the electrolyte cost per ton of C_2H_4, we calculate the $\text{CRF}_{\text{electrolyte}}$ by assuming an electrolyte lifetime of 1 year.

$$\mathrm{CRF_{electrolyte}} = \frac{i(1+i)^{lifetime}}{(1+i)^{lifetime}-1} = \frac{0.07(1.07)^1}{1.07^1-1} = 1.07$$

$$\text{Electrolyte cost } (\frac{\$}{\mathrm{ton_{C_2H_4}}}) = \frac{\mathrm{CRF_{electrolyte}} \times \mathrm{Cost_{electrolyte}}\ (\$)}{\text{Capacity factor} \times 365\frac{\text{days}}{\text{year}} \times \mathrm{C_2H_4}\text{ production } (\frac{\text{ton}}{\text{day}})}$$

$$\mathrm{CO_2}\text{ cost } (\frac{\$}{\mathrm{ton_{C_2H_4}}}) = \frac{\text{Molar mass}_{\mathrm{CO_2}}\ (\frac{\mathrm{g}}{\mathrm{mol}})}{\text{Molar mass}_{\mathrm{C_2H_4}}\ (\frac{\mathrm{g}}{\mathrm{mol}})} \times \text{Molar ratio } (\frac{\mathrm{CO_2}}{\mathrm{C_2H_4}}) \times \mathrm{CO_2}\text{ price } (\frac{\$}{\mathrm{ton_{CO_2}}})$$

Balance of plant and installation Costs:

All capital costs are scaled to estimate the price of peripheral equipment for the electrolyzer and separation units. A balance of plant of 50% and a Lang factor of 1 are assumed for all calculations.[17] Total capital costs are obtained by summing the costs of the electrolyzer, catalyst & membrane, and separation capital.

$$\text{Total capital costs} = \text{Electrolyzer cost} + \text{C\&M cost} + \text{PSA capital cost}$$

$$\text{BoP } (\frac{\$}{\mathrm{ton_{C_2H_4}}}) = \text{BoP Factor} \times \text{Total Capital Costs } (\frac{\$}{\mathrm{ton_{C_2H_4}}})$$

$$\mathrm{Cost_{Installation}}\ (\frac{\$}{\mathrm{ton_{C_2H_4}}}) = \text{Lang factor} \times \text{Total capital costs } (\frac{\$}{\mathrm{ton_{C_2H_4}}})$$

Other operating cost:

To consider the additional operating costs associated with running a plant, such as labor and maintenance, the other operating coat is assumed to be 10% of the electricity cost.[18]

$$\text{Other operating costs } (\frac{\$}{\mathrm{ton_{C_2H_4}}}) = \text{Cost of electricity } (\frac{\$}{\mathrm{ton_{C_2H_4}}}) \times 10\%$$

Energy efficiency:

The full-cell energy efficiencies (EE, %) was calculated as follows:

$$EE = \frac{(1.23\ V - E_i) \times FE_i}{E_{\mathrm{cell}}}$$

E_i and FE_i are the thermodynamic potential (*versus* RHE) and Faradaic efficiency for product i (E_i = -0.08 V for C_2H_4), respectively, and E_{cell} is the full cell voltage applied to the MEA.

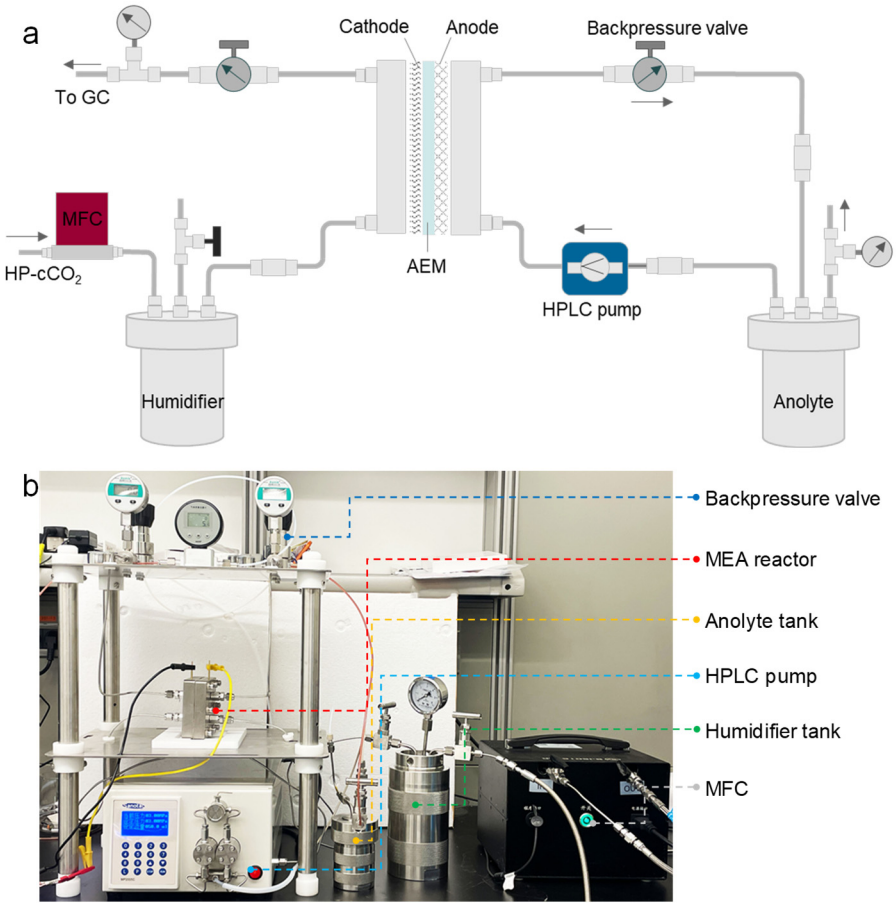

Supplementary Fig. 1 | Electrochemical apparatus. (a) Schematic and (b) photograph of the high-pressure MEA system. AEM, anion-exchange membrane. HPLC, high performance liquid chromatography. MFC, mass flow controller.

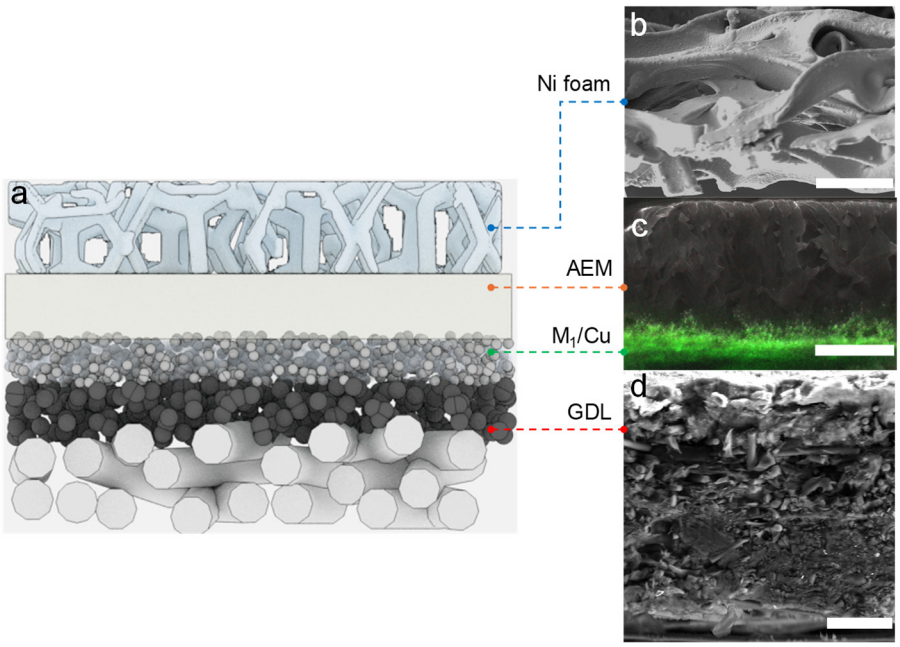

Supplementary Fig. 2 | Membrane electrode structure. (a) Schematic of the MEA. SEM images of (b) Ni foam anode, (c) M_1/Cu catalyst coated AEM, and (d) GDL. The green pixels in (c) represent the Cu element. Scale bars, 100 μm (b), 10 μm (c) and 50 μm (d).

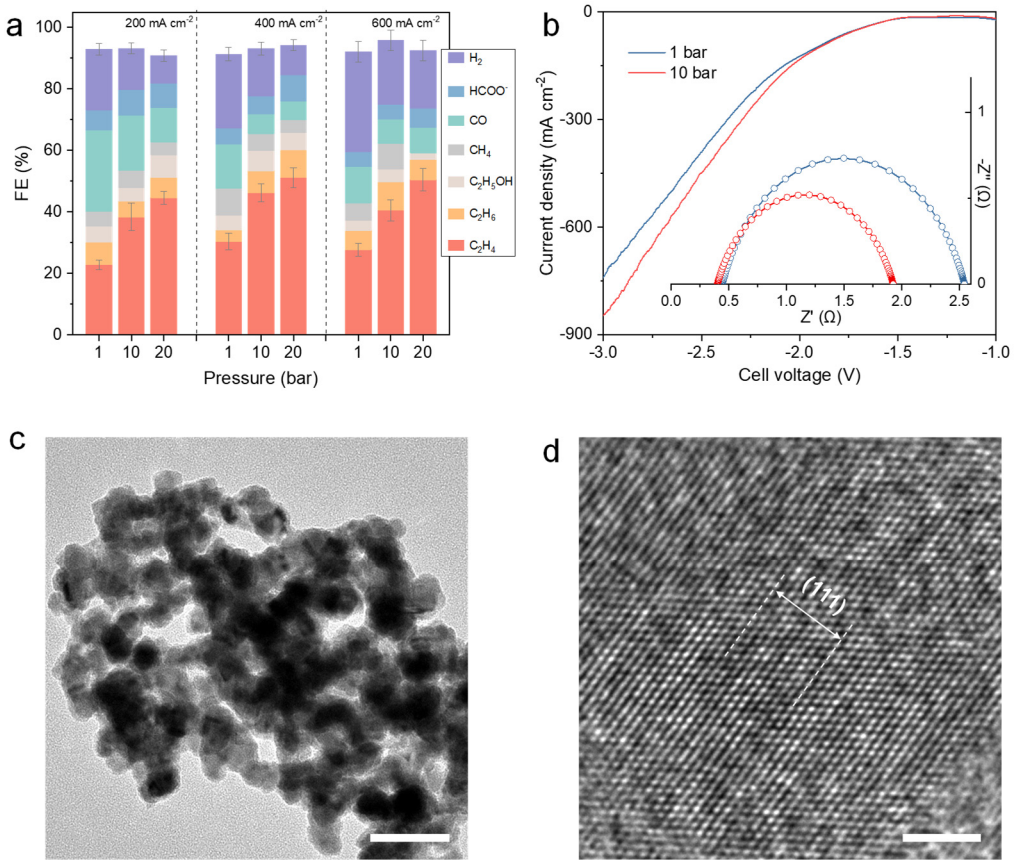

Supplementary Fig. 3 | CO_2R on Cu. (a) FEs toward CO_2R products and H_2 on Cu under different pressures and current densities. (b) LSV curves of Cu catalyst under different CO_2 pressures. The scan rate is 50 mV s^{-1}. The inset shows the electrochemical impedance spectroscopy (EIS) spectra of Cu with a frequency range from 100 kHz to 0.01 Hz recorded at a cell voltage of 1.8V under different pressures. (c) TEM and (d) HRTEM image of the Cu catalyst. Scale bars, 50 nm (c) and 2 nm (d). Error bars represent the standard deviation of three independent measurements.

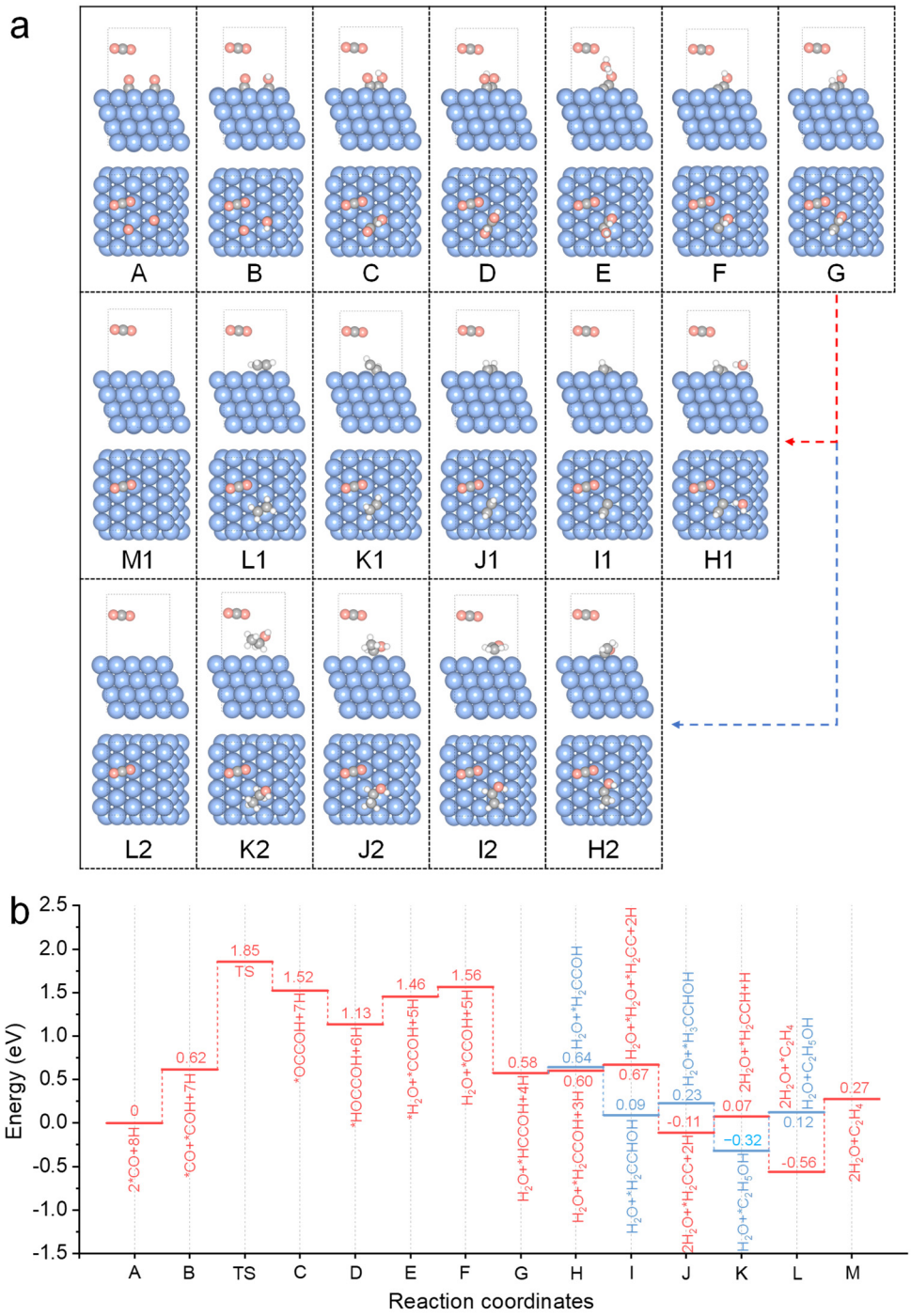

Supplementary Fig. 4 | DFT simulations of ambient pressure CO_2R mechanism. (a) Optimized configurations of intermediates on Cu(111) for CO-to-C_2H_4 (A-M1) and CO-to-C_2H_5OH (A-L2) with a CO_2 density of 1 nm^{-3} in the vacuum layer, Cu: blue; O: red; C: gray; H: white. (b) The corresponding Gibbs free energy diagrams.

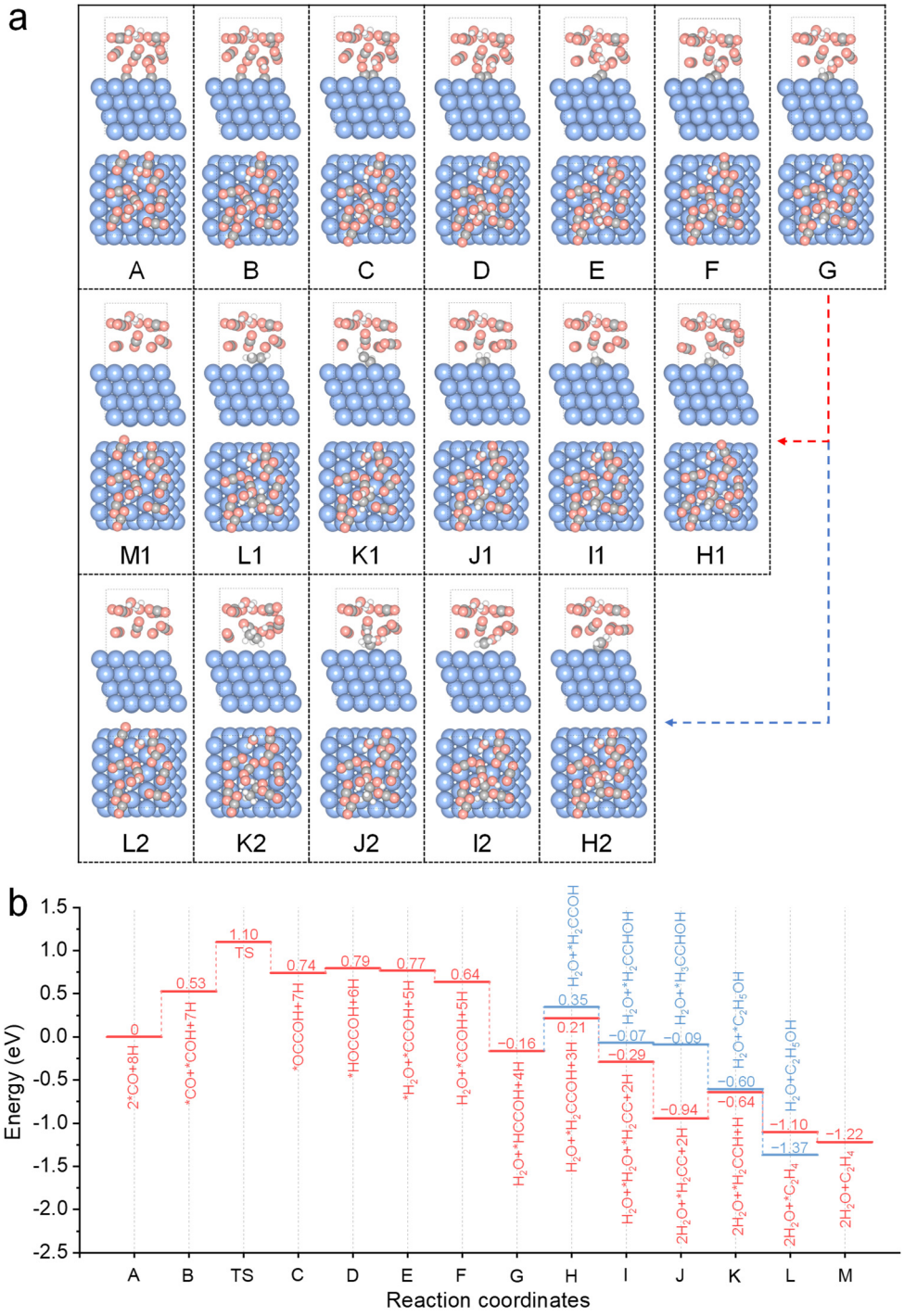

Supplementary Fig. 5 | DFT simulations of high pressure CO_2R mechanism. (a) Optimized configurations of intermediates on Cu(111) for CO-to-C_2H_4 (A-M1) and CO-to-C_2H_5OH (A-L2) with a CO_2 density of 10 nm^{-3} in the vacuum layer, Cu: blue; O: red; C: gray; H: white. (b) The corresponding Gibbs free energy diagrams.

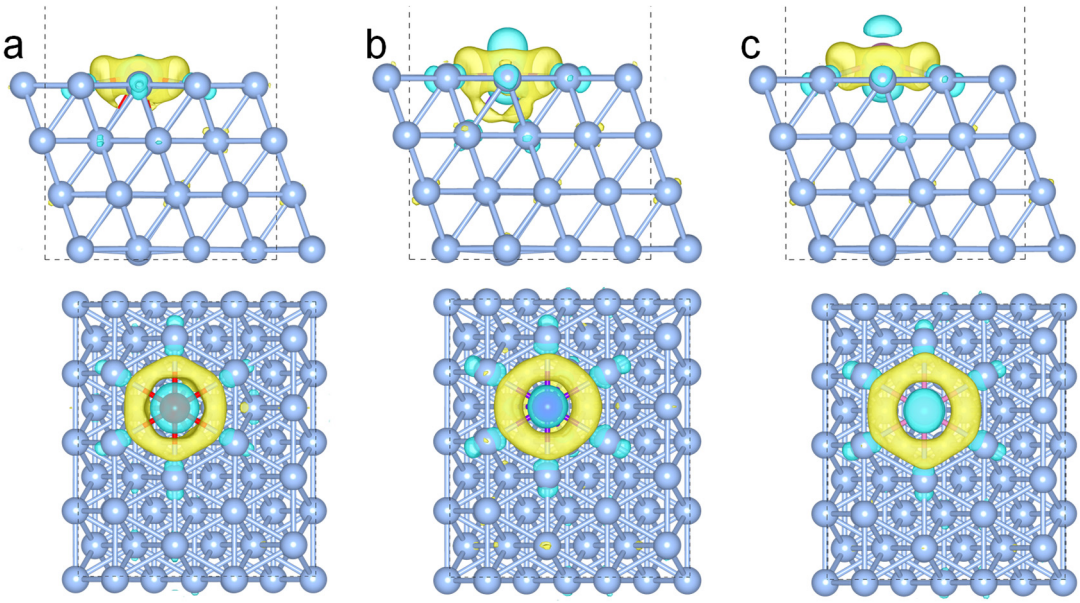

Supplementary Fig. 6 | Charge density difference. Charge density difference plots of (a) Ag_1/Cu, (b) Al_1/Cu and (c) In_1/Cu catalysts illustrating the charge transfer between Cu and M atoms during the doping and binding. Side view (upper) and top view (lower). The yellow and cyan represent the accumulation and depletion regions of electrons, respectively.

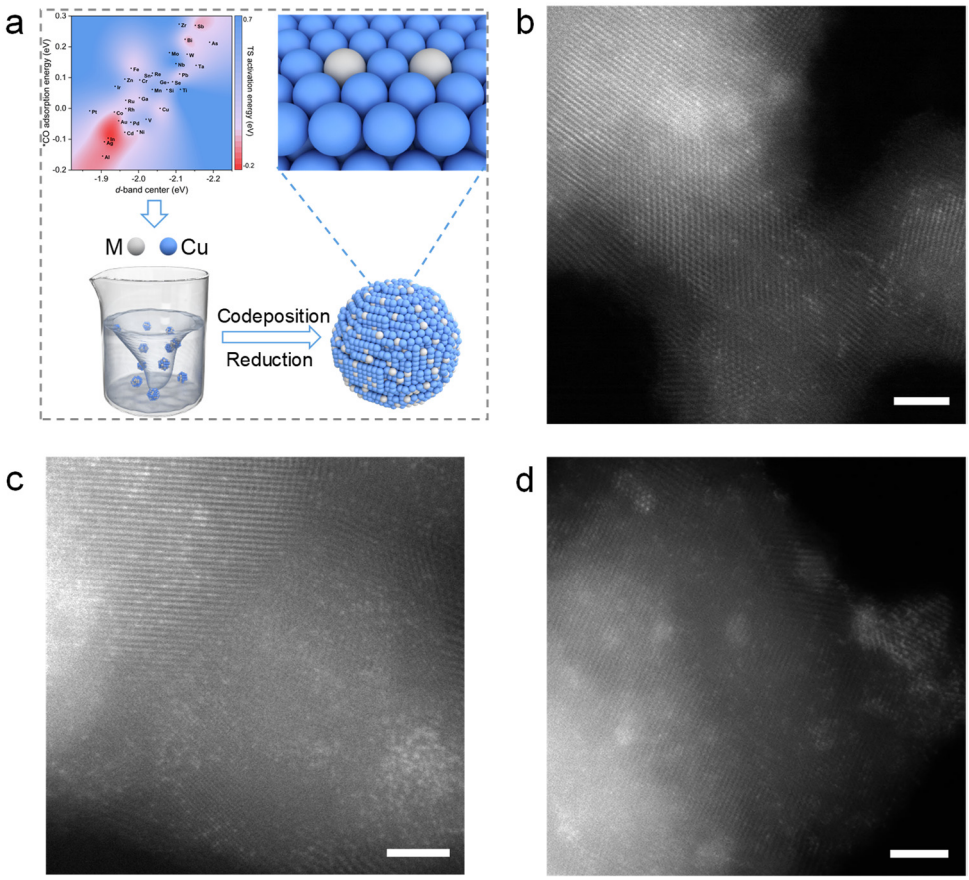

Supplementary Fig. 7 | Catalyst synthesis. (a) Schematic of the synthesis procedure for M_1/Cu catalysts. STEM images of the In_1/Cu catalysts with In atomic proportions of (b) 2%, (c) 3% and (d) 4%. Scale bars, 2 nm (b-d).

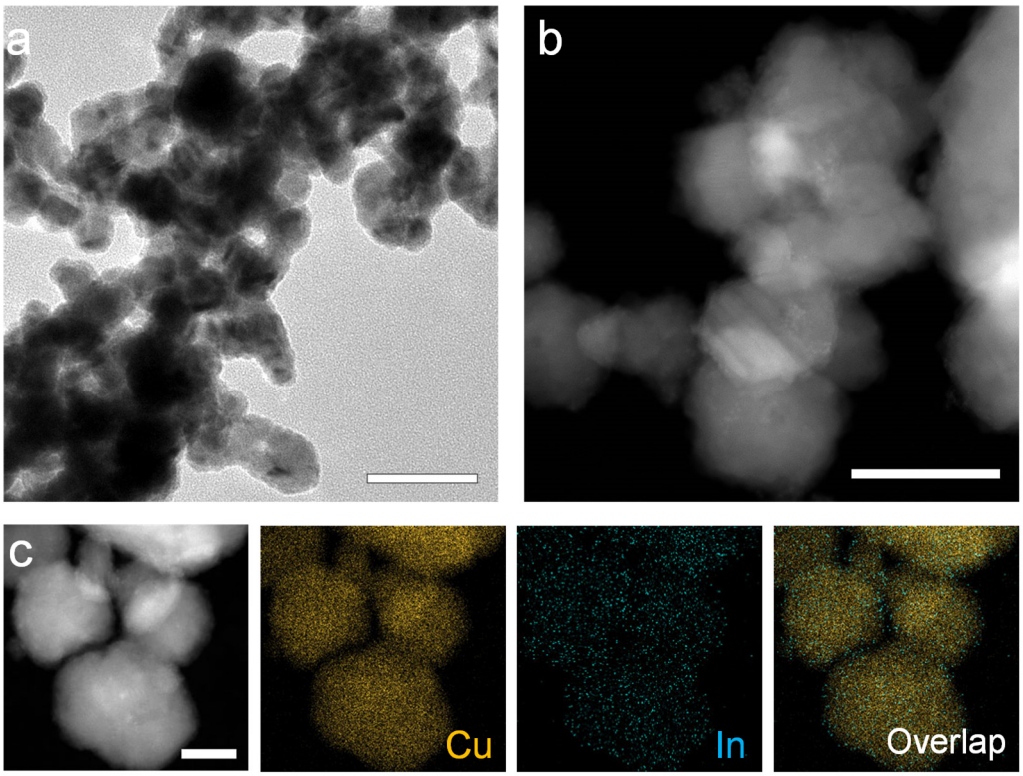

Supplementary Fig. 8 | Characterization of In_1/Cu catalyst. (a) TEM image, (b) STEM image, and (c) STEM mapping of the In_1/Cu catalyst. Scale bars, 50 nm (a), 50 nm (b), 20 nm (c).

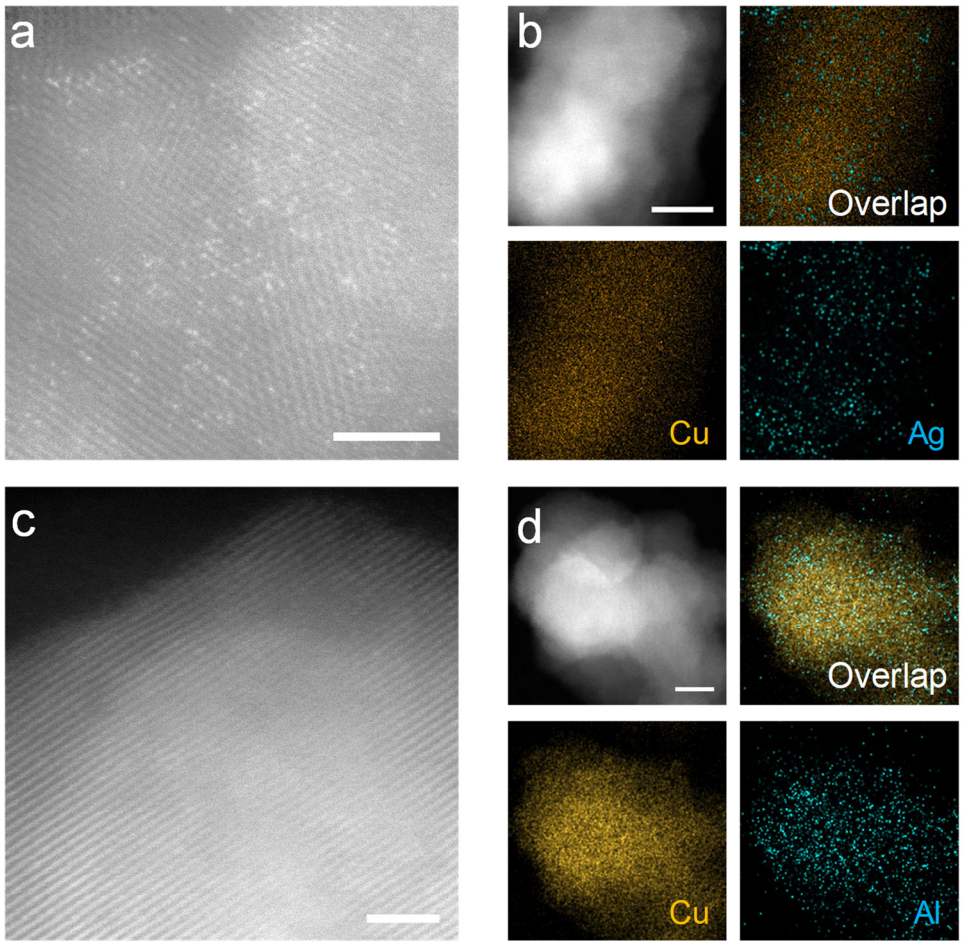

Supplementary Fig. 9 | Characterization of Ag_1/Cu and Al_1/Cu catalysts. (a) STEM image and (b) STEM-EELS mapping of the Ag_1/Cu catalyst. (c) STEM image and (d) STEM-EELS mapping of the Al_1/Cu catalyst. Scale bars, 2 nm (a), 5 nm (b), 2 nm (c) and 5 nm (d).

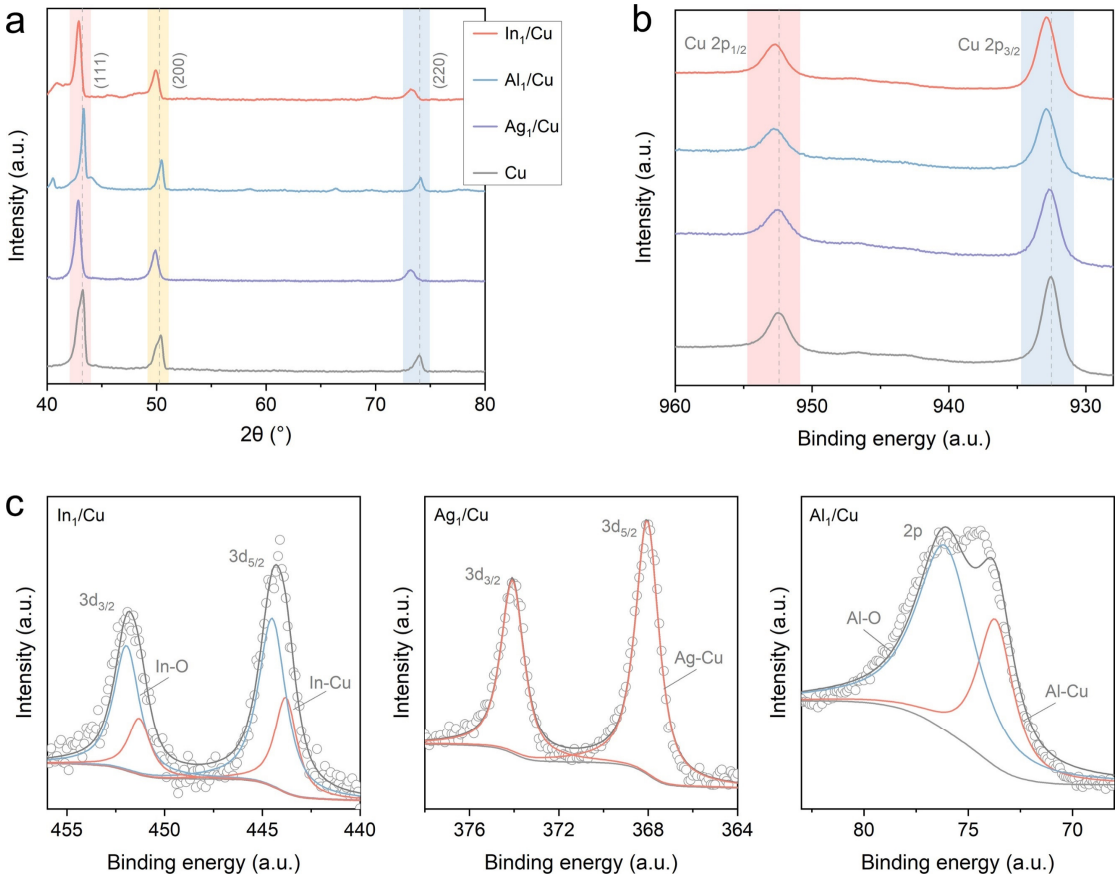

Supplementary Fig. 10 | Structure characterization of M_1/Cu catalysts. (a) XRD and (b) XPS spectra of In_1/Cu, Ag_1/Cu, Al_1/Cu and Cu catalysts. (c) In 3d, Ag 3d and Al 2p XPS spectra.

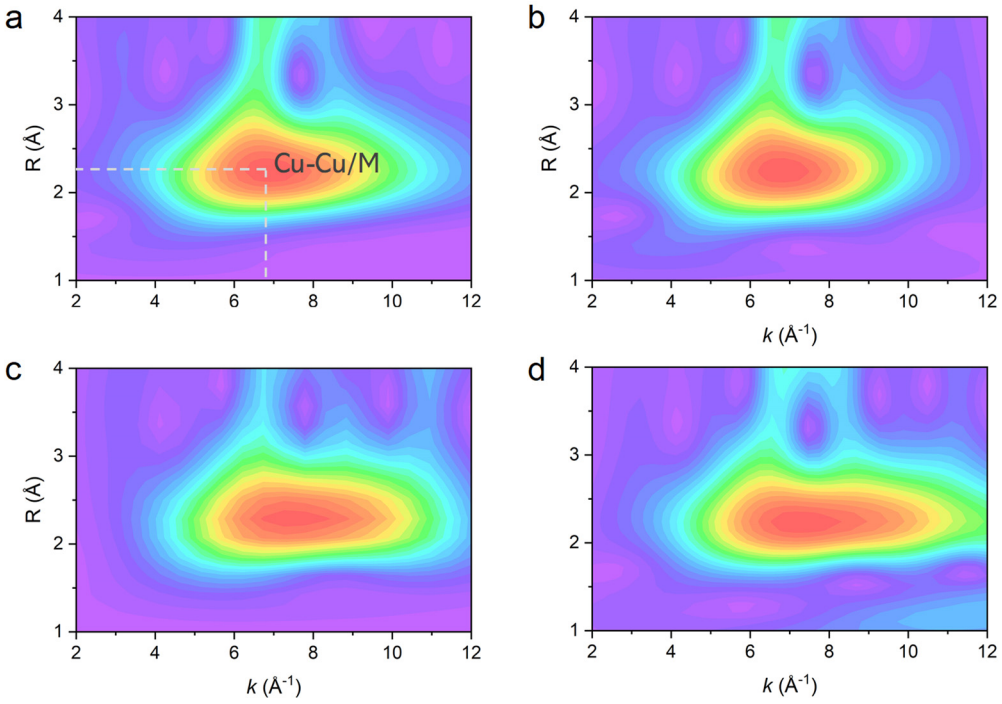

Supplementary Fig. 11 | Cu K-edge XAS analysis. Cu K-edge wavelet-transformed (WT) EXAFS spectra of (a) Cu, (b) Al_1/Cu, (c) Ag_1/Cu and (d) In_1/Cu catalysts.

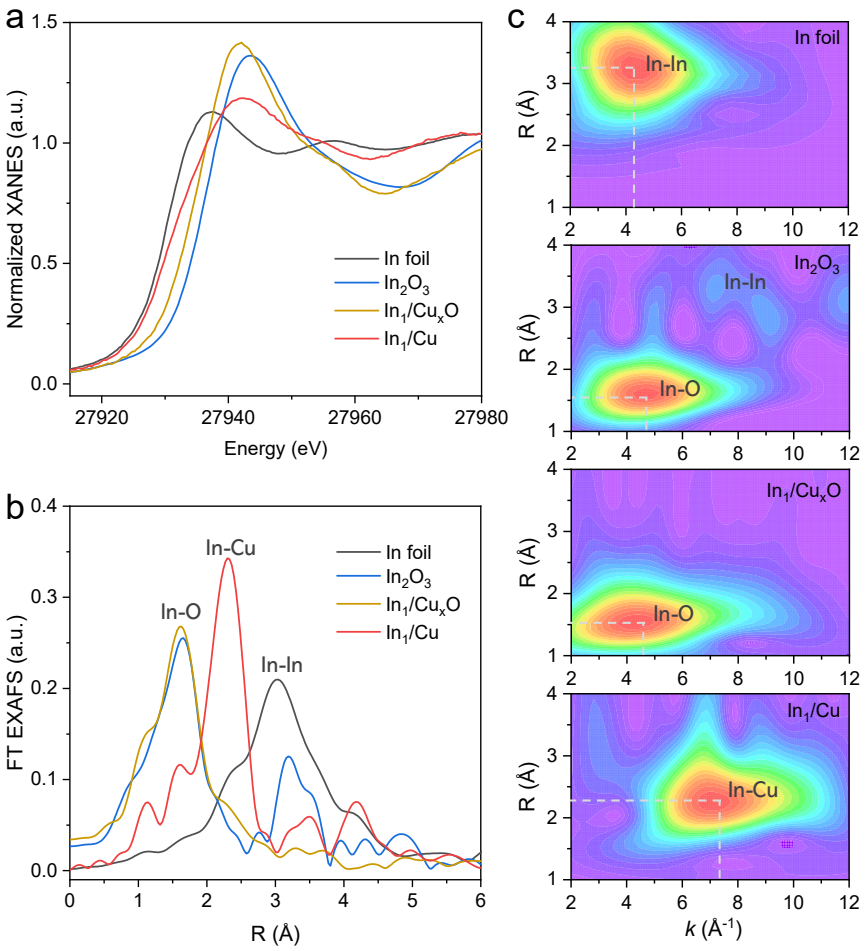

Supplementary Fig. 12 | In K-edge XAS analysis. (a) XANES, (b) Fourier-transformed (FT) EXAFS and (c) WT-EXAFS spectra of In_1/Cu catalyst, with In foil, In_2O_3 and In_1/Cu_xO as references.

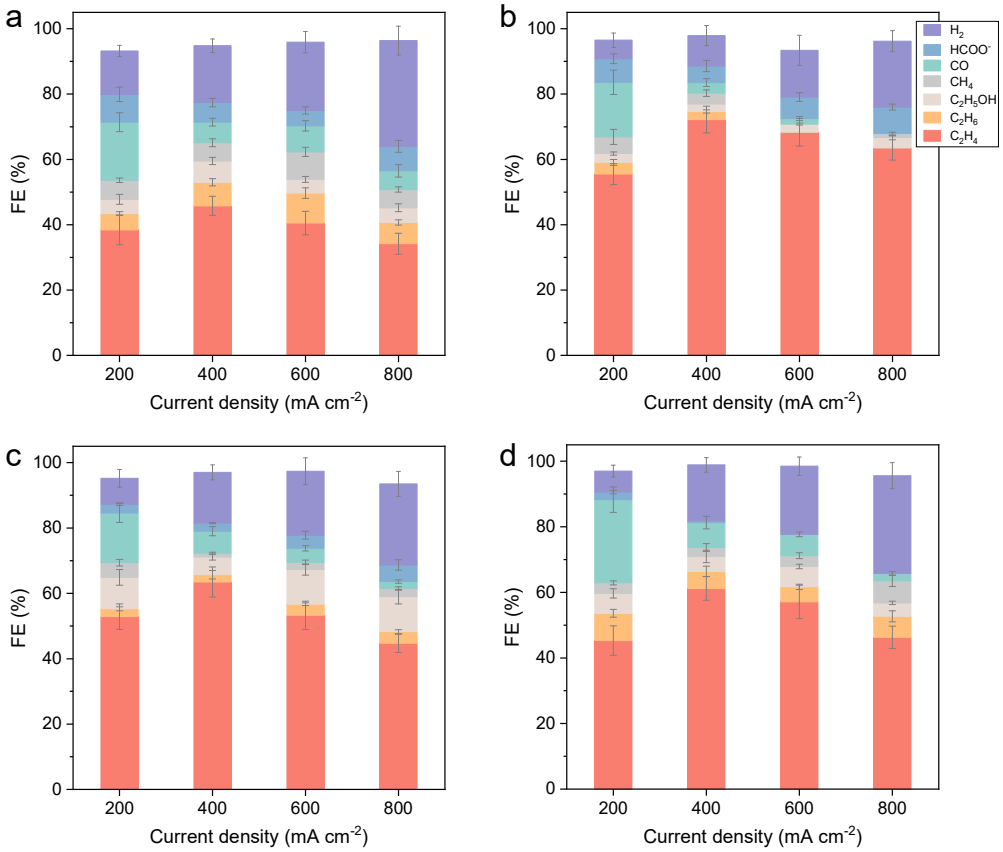

Supplementary Fig. 13 | CO_2R on M_1/Cu catalysts under pressure. FEs toward CO_2R products and H_2 on (a) Cu, (b) In_1/Cu, (c) Al_1/Cu and (d) Ag_1/Cu catalysts under 10 bar at different current densities. Error bars represent the standard deviation of three independent measurements.

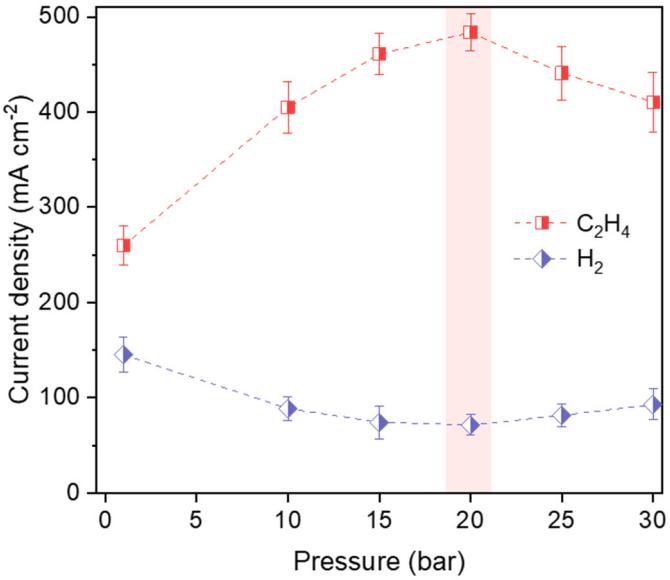

278

279 **Supplementary Fig. 14 | CO_2R performance of In_1/Cu catalyst.** C_2H_4 and H_2 partial current
280 densities on In_1/Cu catalyst under different pressures at a constant current density of 600 mA cm^{-2}.
281

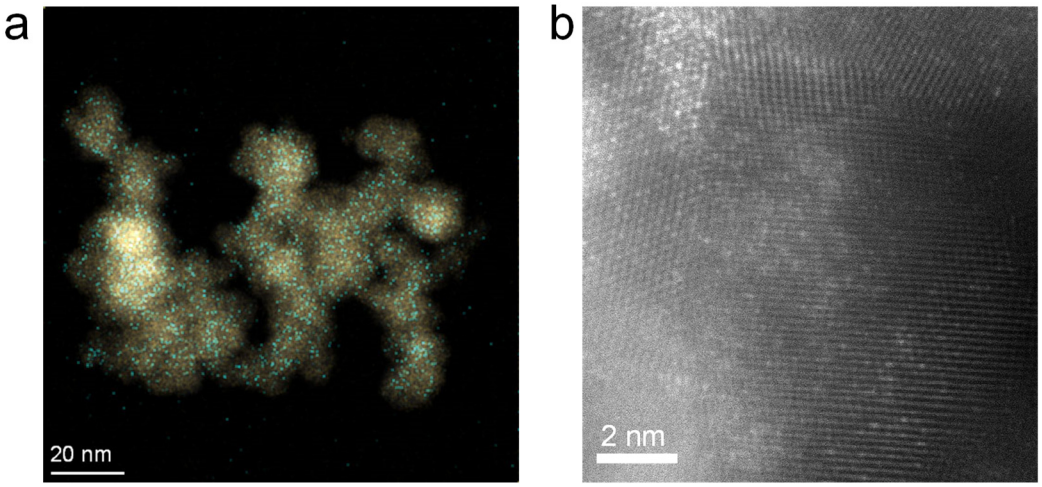

Supplementary Fig. 15 | STEM images of In_1/Cu catalyst after CO_2R. (a) STEM-EELS mapping and (b) STEM image of the In_1/Cu catalyst after CO_2R. The yellow and blue pixels in (a) represent the Cu and In elements, respectively.

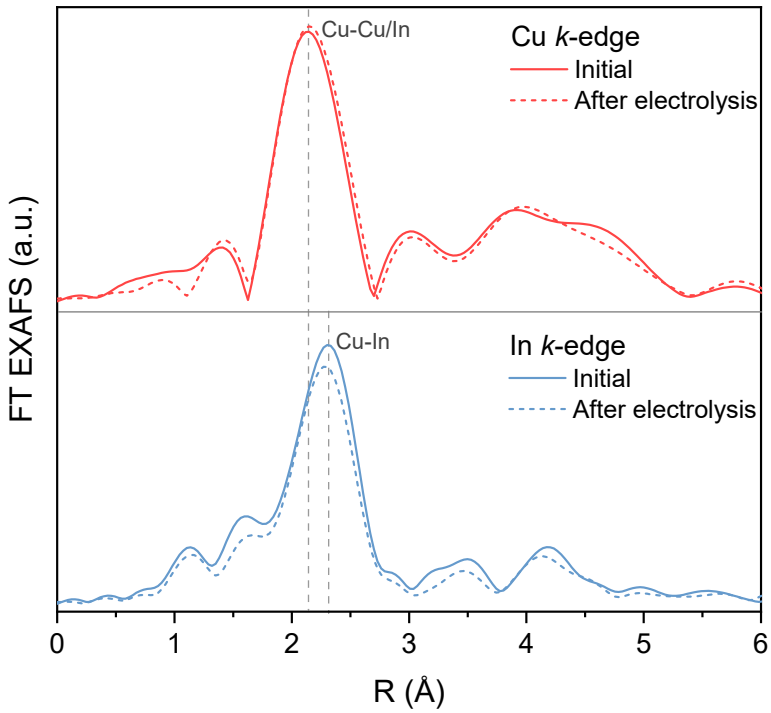

287

288 **Supplementary Fig. 16 | XAS analysis of In_1/Cu catalyst after CO_2R.** FT-EXAFS spectra of
289 In_1/Cu catalyst at Cu and In K-edges before and after CO_2R.

290

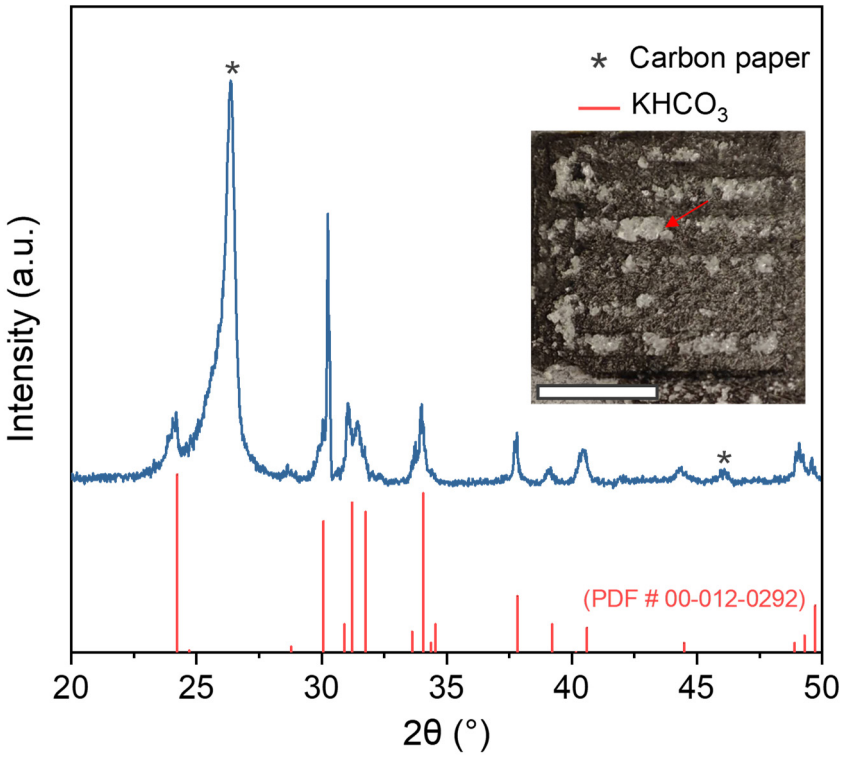

Supplementary Fig. 17 | Analysis of precipitation. XRD of the bicarbonate salt. Insert: photograph of precipitated salt on the back side of GDL. Scale bar, 5 mm.

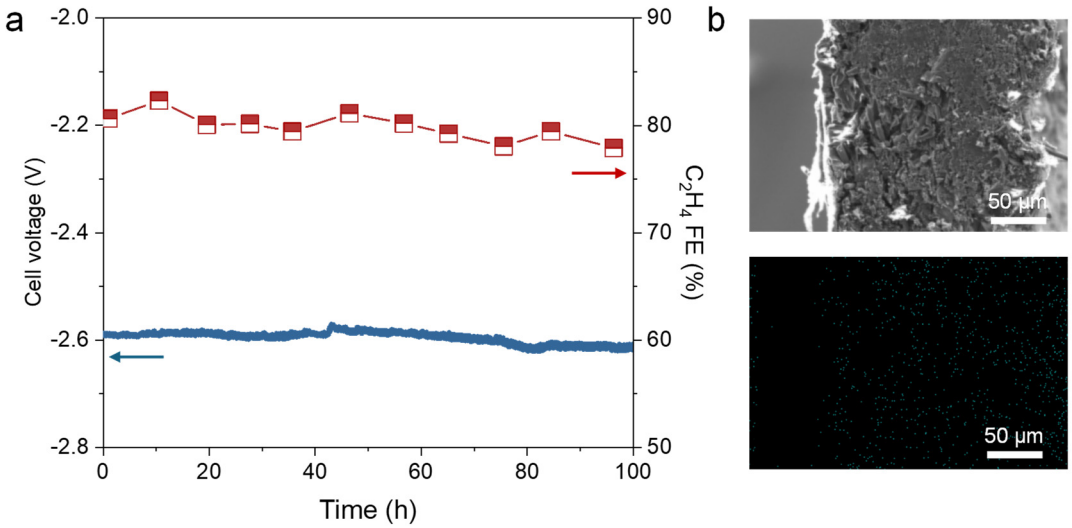

295

296 **Supplementary Fig. 18 | CO_2R on In_1/Cu using 1 M $KHCO_3$ anolyte.** (a) C_2H_4 FE and
297 chronopotentiogram of In_1/Cu under 20 bar at 600 mA cm^{-2}. (b) Cross-sectional SEM image (upper)
298 and EDS mapping of K^+ (lower) for the cathode after electrolysis.

299

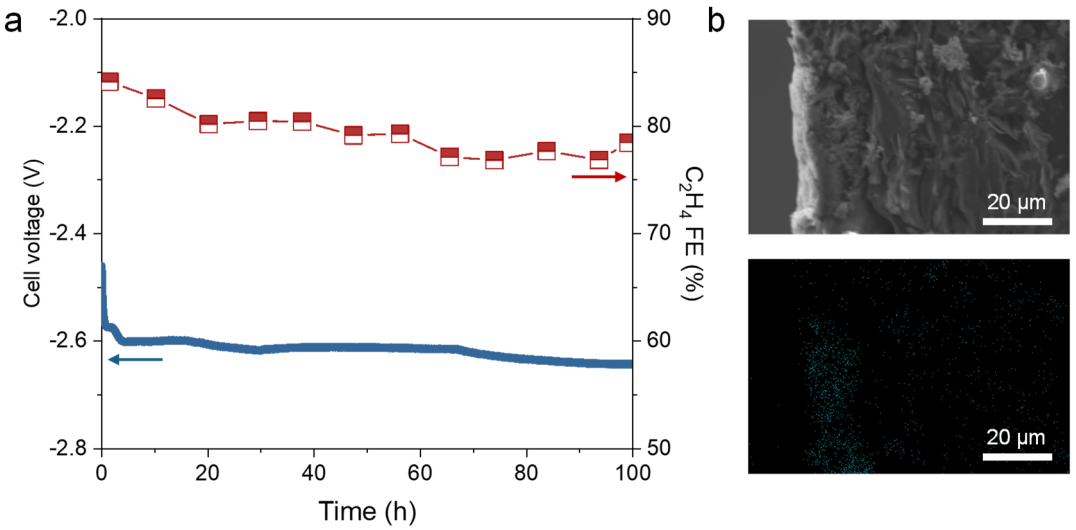

Supplementary Fig. 19 | CO_2R on In_1/Cu using 1 M KOH anolyte. (a) C_2H_4 FE and chronopotentiogram of In_1/Cu under 20 bar at 600 mA cm^{-2}. (b) Cross-sectional SEM image (upper) and EDS mapping of K^+ (lower) for the cathode after electrolysis.

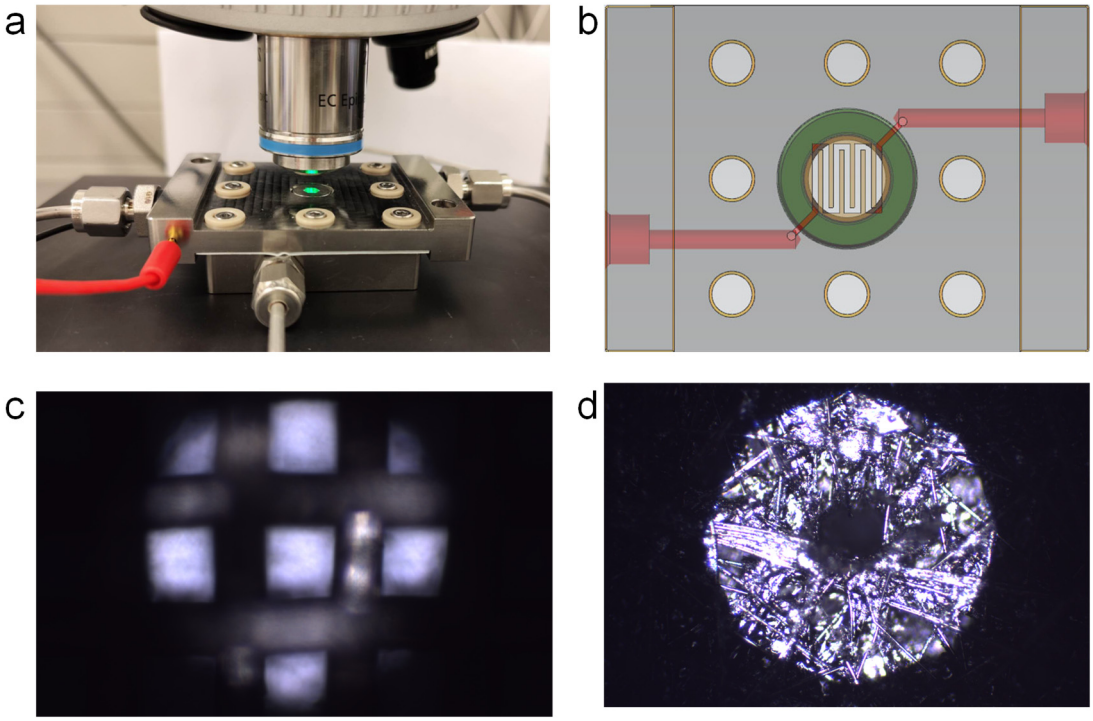

Supplementary Fig. 20 | *Operando* Raman apparatus. (a) Photograph and (b) schematic of the MEA customized for *operando* Raman spectroscopy. Optical microscopic images of the (c) IrO_2/Ti meshed anode and (d) cathode GDL with micrometer-scale pores.

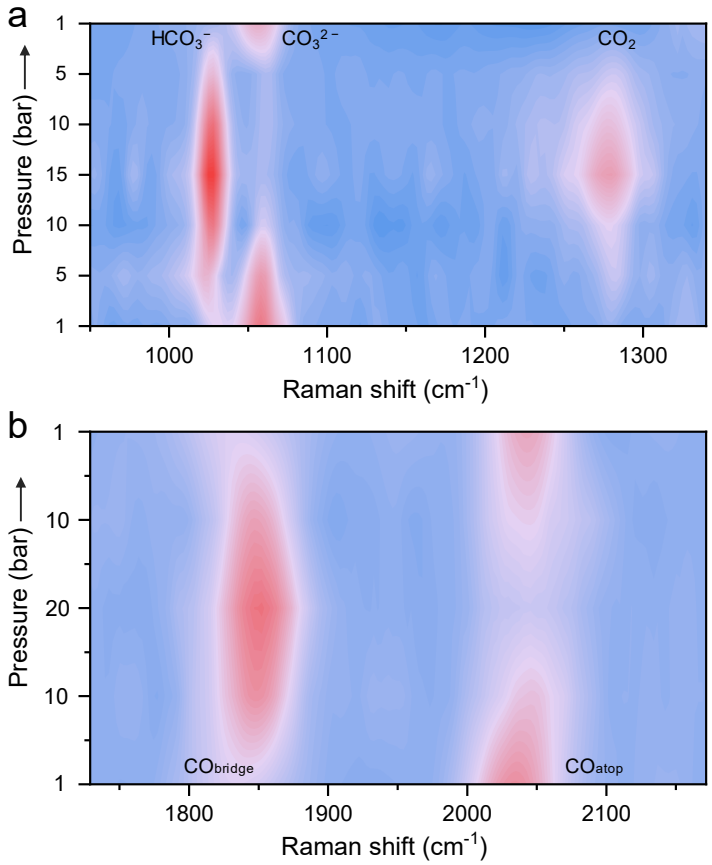

310

311 **Supplementary Fig. 21 | *Operando* Raman spectra.** Pressure-dependent *operando* Raman spectra
312 of the (a) cathode-membrane interface acquired from the anode side and (b) catalyst layer acquired
313 from the cathode side. The trends remained the same for both forward and reverse pressure scans.

314

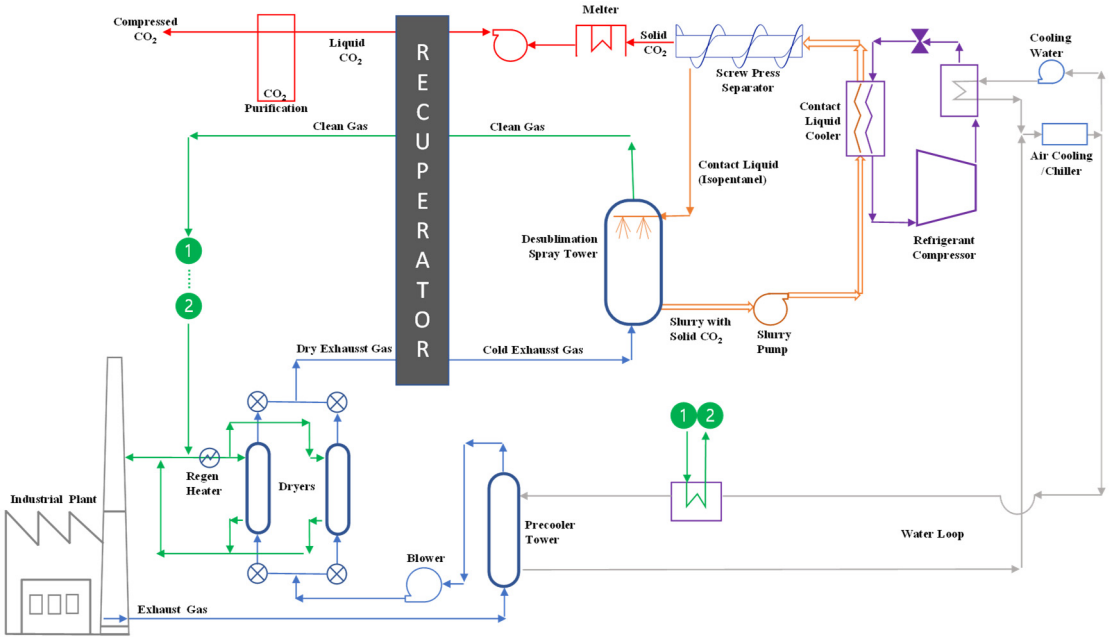

Supplementary Fig. 22 | Schematic of CCC process. A process flow diagram of CCC showing main subsystems. The flue gases underwent a precooling → drying → freezing → compressing process. Despite major advances in existing CO_2 capture technologies, such as amine scrubbing[23], chemical looping[24], and solid sorbents[25], the industry is actively seeking a solution that is more energy-efficient and cost-effective[26]. CCC technology emerges as an appealing option: (i) the CCC rig can capture 90–99% CO_2 from typical coal-fired flue gases, and output CO_2 (10−73 bar, -35−28 °C) with 99.999% purity[2,26]; (ii) its operation is based on heat exchange, without the need of expensive air separation units or CO_2 absorbents. Consequently, CCC curtails 50% energy demand and 20% cost compared to conventional CO_2 chemisorption methods; and (iii) the heat exchangers in CCC are electric-driven – that means, CCC could be powered solely by renewable electricity. The pressurization, from an energy perspective, consumes less than 3% of the total energy input to the CCC rig[27]. It is worth noting that the pressurization typically accounts for approximately 20% of the total energy consumption in amine-based CO_2 capture systems. C_2H_4 separation from the high-pressure CO_2R effluent was conducted on a lab-scale cryogenic CO_2 capture apparatus consisting of the same components.

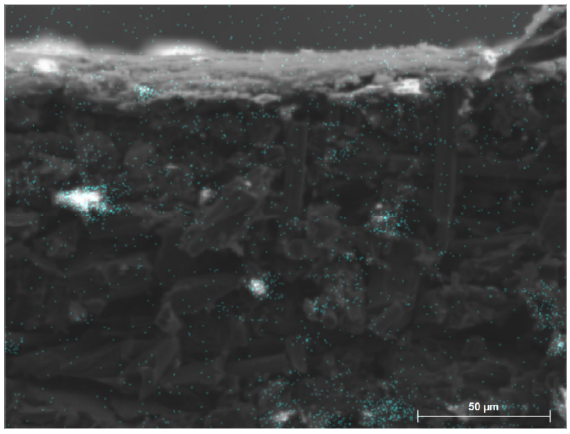

Supplementary Fig. 23 | Cross-sectional SEM image of the cathode with overlaid EDS mapping of K^+ after 1,500-hour prolonged electrolysis of 20 bar HP-cCO_2 at 600 mA cm^{-2}.

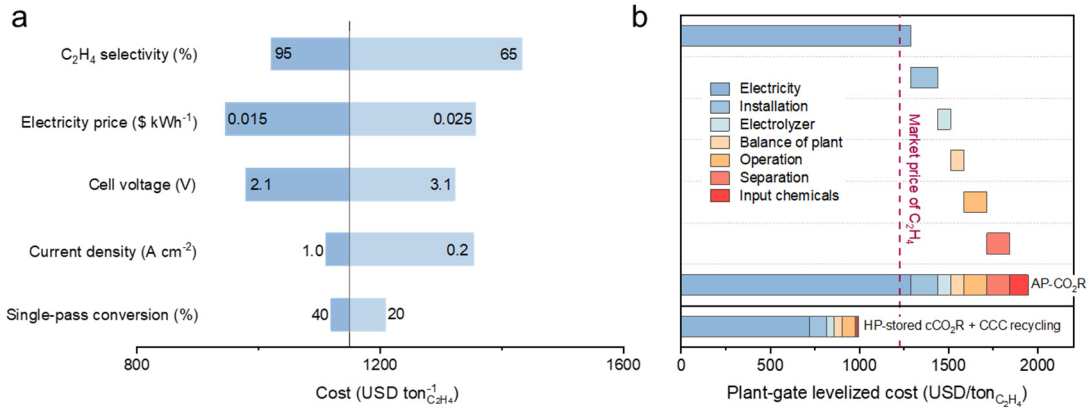

Supplementary Fig. 24 | TEA analysis. (a) Sensitivity analysis, (b) TEA showing the profit and cost breakdown of electrochemically producing C_2H_4 using our proof-of-concept versus ambient pressure CO_2R (AP-CO_2R).

Supplementary Table 1 | *CO adsorption energy on different M_1/Cu.

Adsorption energy (eV)	*CO on M site	*CO on Cu site
In_1/Cu	0.39	-0.89
Ag_1/Cu	-0.05	-0.92
Al_1/Cu	-0.01	-0.99

Supplementary Table 2 | Energy barriers of C-C coupling.

	C-C coupling configuration	Averaged *CO adsorption energy (eV)	C-C coupling energy barrier (eV)
Ambient pressure	CO_{atop}-CO_{atop}	-0.97791	0.44154
	CO_{atop}-CO_{bridge}	-1.01289	0.3493
	CO_{bridge}-CO_{bridge}	-1.03666	0.59055
High pressure	CO_{atop}-CO_{atop}	-0.91779	0.30243
	CO_{atop}-CO_{bridge}	-0.94372	0.17013
	CO_{bridge}-CO_{bridge}	-0.95846	0.3756

347 **Supplementary Table 3 | Summary of the CO_2R performance in gas-fed MEAs.**

Catalysts	Membrane	Electrolyte	Pressure	Cell voltage (V)	Current density (mA cm^{-2})	Products	FE (%)	Duration (h)	Ref.
In_1/Cu	**AEM**	**0.1 M $KHCO_3$**	**20 bar**	**2.75**	**600**	**C_2H_4**	**85**	**>1500**	**This work**
				3.15	**1000**	**C_2H_4**	**72**	**–**	
Cu/tetrahydro-bipyridine film	AEM	0.1 M $KHCO_3$	1 bar	3.65	120	C_2H_4	72	190	*Nature* **577**, 509–513 (2020)
Surface-step-rich Cu	AEM CEM	H_2O	1 bar	~4.4	333	C_2H_4	~50	1000	*Nat. Energy* **9**, 81–91 (2024)
Cu/aryl diazonium	AEM	0.5 M $KHCO_3$	1 bar	3.55	250	C_2H_4	~83	120	*Nat. Energy* **9**, 422–433 (2024)
Cu/quasi-graphitic C	AEM	0.1 M $KHCO_3$	1 bar	3.6	~100	C_2H_4	~62	180	*Nat. Commun.* **12**, 3765 (2021)
Cu NPs (250 nm)	AEM	0.1 M $KHCO_3$	1 bar	3.75	120	C_2H_4	~40	100	*Joule* **3**, 2777-2791 (2019)
Porous Cu	AEM	H_2O	1 bar	3.65	900	C_2H_4	46.6	–	*Nat. Energy* **7**, 835–843 (2022)
Sputtered Cu NPs	AEM	0.1 M $KHCO_3$	1 bar	3.9	~200	C_2H_4	~55	60	*Science* **367**, 661-666 (2020)
Sputtered Cu/CTPI	AEM	0.1 M $KHCO_3$	1 bar	~3.6	220	C_2H_4	63	100	*ACS Energy Lett.* **5**, 2811–2818 (2020)
Cu/FeTPP[Cl]	AEM	0.1 M $KHCO_3$	1 bar	3.7	120	C_2H_5OH	41	12	*Nat. Catal* **3**, 75–82 (2020)
Electrodeposited Cu	AEM	0.15 M $KHCO_3$	1 bar	3.7	~300	C_2H_4	~60	65	*Nat. Catal* **3**, 98–106 (2020)
N-C/Cu	AEM	0.2 M $KHCO_3$	1 bar	3.67	~160	C_2H_5OH	52	15	*Nat. Energy* **5**, 478–486 (2020).
CuO nanosheets	AEM	0.1 M KOH	1 bar	~3.5	600	C_2H_4	52.5	–	*Nat. Nanotechnol.* **18**, 299–306 (2023)
DVL-Cu NPs	AEM	0.5 M $KHCO_3$	1 bar	~3.45	250	C_2H_4	~71	–	*Nat. Commun.* **13**, 1877 (2022)
Cu(OH)BTA	CEM	1 M KOH	1 bar	3.8	~237	C_2H_4	52	67	*Nat. Commun.* **14**, 474 (2023)
Cu(100)-rich films	AEM	0.1 M $KHCO_3$	1 bar	~2.5	120	C_2H_4	555.8	4.5	*Nat. Commun.* **12**, 5745 (2021)
Defect-Site-Rich Cu	AEM	0.1 M $KHCO_3$	1 bar	3.5	200	C_2H_5OH	~60	30	*Joule* **5**, 429–440 (2021)
Cu/PCRL	CEM	0.01 M H_2SO_4	1 bar	~3.9	100	C_2H_4	~37	9	*ACS Energy Lett.* **6**, 2952–2959 (2021)
Low-coordinated Cu	AEM	0.05 $KHCO_3$	1 bar	~4	190	CH_4	~56	110	*Nat. Commun.* **12**, 2932 (2021)
La_5Cu_{95}	AEM	1 M KOH	1 bar	3.4	~400	CH_4	45.4	–	*J. Am. Chem. Soc.* 145, 6622 (2023)
Ag/PTFE	CEM	0.01 M H_2SO_4 0.01 M Cs_2SO_4	1 bar	~3.75	60	CO	~40	50	*ACS Energy Lett.* **7**, 4224–4231 (2022)
Ag NPs	AEM	1 M KOH	4-6 bar	3	~300	CO	~95	10	*ACS Energy Lett.* **4**, 1770–1777 (2019)
Ag NPs	BPM	1 M KOH	3 bar	~3.5	100	CO	83	120	*ACS Energy Lett.* **9**, 2800–2806 (2024)

Ni–N–C	BPM	0.5 M K_2SO_4 H_2SO_4	5 bar	~3.7	500	CO	~94	8	*Energy Environ. Sci.* **16**, 1502-1510 (2023)
Ni–N–C	AEM	0.1 M $KHCO_3$	1 bar	3.52	80	CO	~93	273	*Energy Environ. Sci.* **16**, 4423-4431 (2023)
Ag NPs	BPM	3 M KOH	1 bar	~3.6	50	CO	68	–	*ACS Energy Lett.* **6**, 4291–4298 (2021)
Ag NPs	AEM	1 M CsOH	1 bar	3.2	~470	CO	~90	200	*Nat. Energy* **6**, 439–448 (2021)
Ag NPs	BPM	H_2O	1 bar	~2.9	300	CO	~70	100	*ACS Appl. Mater. Interfaces* **16**, 24649–24659 (2024)

348

Supplementary references

1. Sun, Y. *et al.* Ultrafast electrodeposition of Ni−Fe hydroxide nanosheets on nickel foam as oxygen evolution anode for energy-saving electrolysis of Na_2CO_3/$NaHCO_3$. *ChemElectroChem* **4**, 1044-1050 (2017).
2. Frankman, D. *et al.* Recent Cryogenic Carbon Capture™ field test results. *SSRN Electronic Journal* (2021).
3. Kresse, G. & Furthmüller, J. Efficiency of ab-initio total energy calculations for metals and semiconductors using a plane-wave basis set. *Comput. Mater. Sci.* **6**, 15-50 (1996).
4. Kresse, G. & Furthmüller, J. Efficient iterative schemes for ab initio total-energy calculations using a plane-wave basis set. *Phys. Rev. B* **54**, 11169-11186 (1996).
5. Kresse, G. & Joubert, D. From ultrasoft pseudopotentials to the projector augmented-wave method. *Phys. Rev. B* **59**, 1758-1775 (1999).
6. Blöchl, P. E. Projector augmented-wave method. *Phys. Rev. B* **50**, 17953-17979 (1994).
7. Perdew, J. P., Burke, K. & Ernzerhof, M. Generalized Gradient Approximation Made Simple. *Phys. Rev. Lett.* **77**, 3865-3868 (1996).
8. Grimme, S., Ehrlich, S. & Goerigk, L. Effect of the damping function in dispersion corrected density functional theory. *J. Comput. Chem.* **32**, 1456-1465 (2011).
9. Chadi, D. J. & Cohen, M. L. Special Points in the Brillouin Zone. *Phys. Rev. B* **8**, 5747-5753 (1973).
10. Wang, V., Xu, N., Liu, J.-C., Tang, G. & Geng, W.-T. VASPKIT: A user-friendly interface facilitating high-throughput computing and analysis using VASP code. *Comput. Phys. Commun.* **267**, 108033 (2021).
11. Yi, W., Tang, G., Chen, X., Yang, B. & Liu, X. qvasp: A flexible toolkit for VASP users in materials simulations. *Comput. Phys. Commun.* **257**, 107535 (2020).
12. Momma, K. & Izumi, F. VESTA 3 for three-dimensional visualization of crystal, volumetric and morphology data. *J. Appl. Crystallogr.* **44**, 1272-1276 (2011).
13. Nørskov, J. K. *et al.* Origin of the Overpotential for Oxygen Reduction at a Fuel-Cell Cathode. *J. Phys. Chem. B* **108**, 17886-17892 (2004).
14. Zhang, J. *et al.* Strong Metal–Support Interaction Boosts Activity, Selectivity, and Stability in Electrosynthesis of H2O2. *J. Am. Chem. Soc.* **144**, 2255-2263 (2022).
15. Deng, W. *et al.* Unraveling the rate-determining step of C_{2+} products during electrochemical CO reduction. *Nat. Commun.* **15**, 892 (2024).
16. Gao, D., Arán-Ais, R. M., Jeon, H. S. & Roldan Cuenya, B. Rational catalyst and electrolyte design for CO_2 electroreduction towards multicarbon products. *Nat. Catal.* **2**, 198-210 (2019).
17. De Luna, P. *et al.* What would it take for renewably powered electrosynthesis to displace petrochemical processes? *Science* **364**, eaav3506 (2019).
18. Jouny, M., Luc, W. & Jiao, F. General techno-economic analysis of CO_2 electrolysis systems. *Ind. Eng. Chem. Res.* **57**, 2165-2177 (2018).
19. Fang, W. *et al.* Low-coordination nanocrystalline copper-based catalysts through theory-guided electrochemical restructuring for selective CO_2 reduction to ethylene. *Angew. Chem. Int. Ed.* **63**, e202319936 (2024).
20. Jin, J. *et al.* Constrained C_2 adsorbate orientation enables CO-to-acetate electroreduction. *Nature* **617**, 724-729 (2023).
21. Sisler, J. *et al.* Ethylene electrosynthesis: A comparative techno-economic analysis of alkaline

vs membrane electrode assembly vs CO_2–CO–C_2H_4 tandems. *ACS Energy Lett.* **6**, 997-1002 (2021).
22. Paturska, A., Repele, M. & Bazbauers, G. Economic assessment of biomethane supply system based on natural gas infrastructure. *Energy Procedia* **72**, 71-78 (2015).
23. Dutcher, B., Fan, M. & Russell, A. G. Amine-based CO_2 capture technology development from the beginning of 2013-a review. *ACS Appl. Mater. Interfaces* **7**, 2137-2148 (2015).
24. Fan, L.-S., Zeng, L., Wang, W. & Luo, S. Chemical looping processes for CO_2 capture and carbonaceous fuel conversion – prospect and opportunity. *Energy Environ. Sci.* **5** (2012).
25. Dunstan, M. T., Donat, F., Bork, A. H., Grey, C. P. & Muller, C. R. CO_2 capture at medium to high temperature using solid oxide-based sorbents: fundamental aspects, mechanistic insights, and recent advances. *Chem. Rev.* **121**, 12681-12745 (2021).
26. Hoeger, C., Burt, S. & Baxter, L. Cryogenic Carbon Capture™ technoeconomic analysis. *SSRN Electronic Journal* (2021).
27. Fazlollahi, F., Bown, A., Ebrahimzadeh, E. & Baxter, L. L. Design and analysis of the natural gas liquefaction optimization process- CCC-ES (energy storage of cryogenic carbon capture). *Energy* **90**, 244-257 (2015).